

---

# 3D PRINTED PROPRIOCEPTIVE SOFT FLUIDIC ACTUATORS WITH GRADED POROSITY

---

**Nick Willemstein**

Department of Biomechanical Engineering  
University of Twente  
Enschede, The Netherlands  
n.willemstein@utwente.nl

**Herman van der Kooij**

Department of Biomechanical Engineering  
University of Twente  
Enschede, The Netherlands  
h.vanderkooij@utwente.nl

**Ali Sadeghi**

Department of Biomechanical Engineering  
University of Twente  
Enschede, The Netherlands  
a.sadeghi@utwente.nl

February 28, 2023

## ABSTRACT

Integration of both actuation and proprioception into the robot body enables sensorized soft actuators that can operate in a closed loop. An interesting class of actuators for this purpose are graded porous actuators, which can be mechanically programmed by their porosity (gradient) and sensorized by using a smart material. Three types of such actuators were 3D printed, namely: a bending finger, contractor, and a three DoF bending segment. Piezoresistive sensing was embedded by printing with a conductive thermoplastic elastomer. A challenge with piezoresistive sensors is to relate the change in resistance to deformation due to their inherent hysteresis and nonlinearity. In this work, an (estimated) Wiener-Hammerstein (WH) model was used to predict the deformation. The bending and contracting actuators showed that the linear and WH models could reach 70+% and 80+% fits, respectively. Thereby indicating that the deformation of the printed actuators could be estimated quite well. Similarly, the 3DoF bending segment showed similar values with the WH model reducing both the fitting and RMS error on average with 20+%. These results indicate that sensorized actuators based on 3D-printed soft structures with a porosity gradient can be mechanically programmed whereas strain estimation can be done using identified Wiener-Hammerstein models.

## 1 Introduction

Soft robotics inherently enable safe cooperation between robots, their environment, and users. Part of this capability is realized by their adaptability due to their reliance on (mechanically) soft structures. This reliance on soft structures instead of rigid mechanical joints is partially inspired by nature, such as seen in the octopus and elephant trunk.

This similarity makes nature a source of inspiration for soft robots<sup>1</sup>. This inspiration led to soft robots such as those that mimic a caterpillar's rolling<sup>2</sup>, an octopus' arm<sup>3</sup>, and skin-inspired sensors (pressure and temperature)<sup>4</sup>. Many biological systems demonstrate adaptive behavior due to their soft skin, body, and muscles. The flexibility of biological muscles has been the inspiration for many soft robotic actuators such as fluidic soft actuators<sup>5,6,7</sup>. These actuators have showcased that a broad range of deformations can be realized such as contraction, twisting, and bending<sup>5,6,7</sup>. However, besides the capability of actuation, biological muscles also have proprioceptive sensors integrated into their structures that enable them to measure the lengthening and force on a muscle<sup>8</sup>. Integration of sensing capability would allow soft actuators to close the loop.

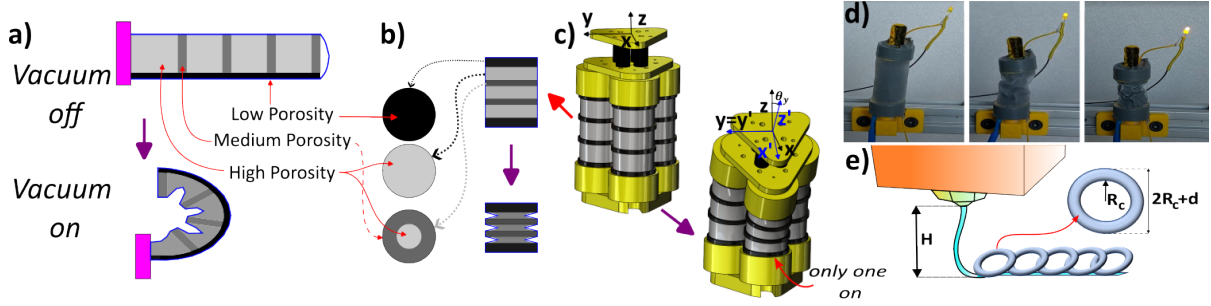


Figure 1: Actuators with porosity gradients: bending actuator (a), contractor (b), 3DoF bending segment (c), effect of compression on resistance of actuator by changing LED brightness (d), and InFoam printing method (e).

To this end, researchers are investigating the integration of sensors into the body of the robot/actuator. Examples include the usage of conductive fibers and the change in inductance<sup>9</sup>. Other examples directly use the change in capacitance/resistance of the actuator itself<sup>10,11</sup>. Another approach is to embed smart materials, such as piezo-resistive material, into the body of the actuator<sup>12,13</sup>.

An interesting class of soft fluidic actuators are porous structures (such as foam). These foam-like structures are inherently flexible, allow for fluid transport, and can be mechanically programmed<sup>14</sup>. Researchers have exploited this property, to realize a broad range of foam actuators, such as contractors, continuum arms, bending fingers, twisting actuators, and pumps<sup>14,15,16,17</sup>.

In addition, foam-based sensors have been investigated using principles such as optical<sup>18</sup>, piezocapacitive<sup>19,20</sup> and piezoresistive<sup>16,21</sup> sensing. By exploiting geometry foam-based sensors can measure a wide range of deformations such as bending, compression, and shear<sup>16,19,21</sup>. In addition, foam-based sensors can be scaled up by patterning multiple electrodes in a matrix format<sup>22</sup>. Lastly, researchers have already demonstrated that sensorized foam can provide proprioceptive data using both optical fibers<sup>18</sup> and piezoresistivity<sup>16</sup>.

To enhance the design flexibility of soft actuators, the fabrication of porous structures that incorporate: a stiffness gradient for deformation programming, a smart material for sensing, and complex geometries need to be possible. One popular approach for manufacturing porous/foam-based actuators in the literature is to use commercial foams as a base material, which are subsequently modified using semi-automatic and manual approaches, which include laser cutting and gluing<sup>15</sup>. This approach has been combined with dip-coating to add the smart material to the structure<sup>16,21</sup>. Another popular method is to use lost sugar/salt casting methods<sup>17,18,19</sup>. One group embedded optical fibers in the casting step for optical sensing<sup>18</sup>. An interesting manufacturing process to fabricate porous structures is 3D printing, as it allows for complex geometries, and a broad range of materials, and can realize composite structures. One approach is to exploit the viscoelastic behavior of the material itself. One example is to exploit liquid rope coiling (i.e. the coiling seen when dropping honey from a height) to create a coiling pattern<sup>23</sup>. The InFoam method<sup>14</sup> used these coils to create pores in a user-defined pattern. Combined with normal printing this allowed for 3D-printed structures with a porosity gradient. Changes in porosity lead to large changes in stiffness (more than one order magnitude<sup>14,24</sup>), which can be used to program the deformation. Examples of actuators based on graded porosity are the bending finger and contractor (Fig. 1(a) and (b)) when actuated with a vacuum the structure collapses leading to a programmed deformation. Furthermore, actuators can be mechanically programmed by changing the porosity of the bending actuator<sup>14</sup> and/or (in general) the spacer location (and number thereof)<sup>25</sup>. Within this work, we combine the InFoam method with a conductive thermoplastic elastomer to print sensorized soft actuators with graded porosity. This approach will be shown to enable both mechanical programming and adjusting the strain-resistance change sensitivity of the contractor. In addition, we demonstrate how the output of the sensorized actuators can be used in conjunction with a Wiener-Hammerstein model for deformation sensing for curvature and translation. Lastly, this combination of printing and system identification will be shown to also apply to the three degrees of freedom (3DoF) bending segment (Fig. 1(c)).

## 2 Materials and Methods

### 2.1 Sensorized Actuators with Graded Porosity

Graded porosity can be exploited to realize actuators with programmable deformation. By fabricating these actuators using a conductive thermoplastic (i.e. carbon-black filled), sensing can be integrated. The conductive thermoplastic enables sensing as the resistance between points in the structure will change due to the deformation history<sup>16,21,26</sup>. The resistance changes can be very significant as seen by the brightness change in Fig. 1(d). An advantage of these sensors

is that resistance measurements require simple electronics. Specifically, the change of resistance is often measured, which is defined as

$$\Delta R = \frac{R - R_0}{R_0} \cdot 100\% \quad (1)$$

Wherein the variables  $\Delta R$ ,  $R$ ,  $R_0$  are the relative change of resistance (%), and the instantaneous and initial (at no strain/stress) resistance ( $\Omega$ ).

However, it is not straightforward to relate the resistance change to a deformation as carbon-black-based sensors are nonlinear. Therefore, a model is necessary to compensate for the nonlinearities. Within this work, a system identification approach is used to convert the resistance change to a deformation. Specifically, a Wiener-Hammerstein model (WH-model) is used (Fig. 2(a)). The WH-model consists of two linear systems and a static nonlinearity in the middle. The combination of linear and nonlinear functions allows the WH-model to capture the inherent nonlinear couplings between resistance change and strain but also take the deformation history into account (to compensate hysteresis). A similar model has shown good results for force sensing resistors<sup>27</sup> but has, to our knowledge, not been applied to strain sensing of soft actuators. Furthermore, we investigate the use of the Wiener-Hammerstein form, which was not (to our knowledge) investigated before for strain estimation.

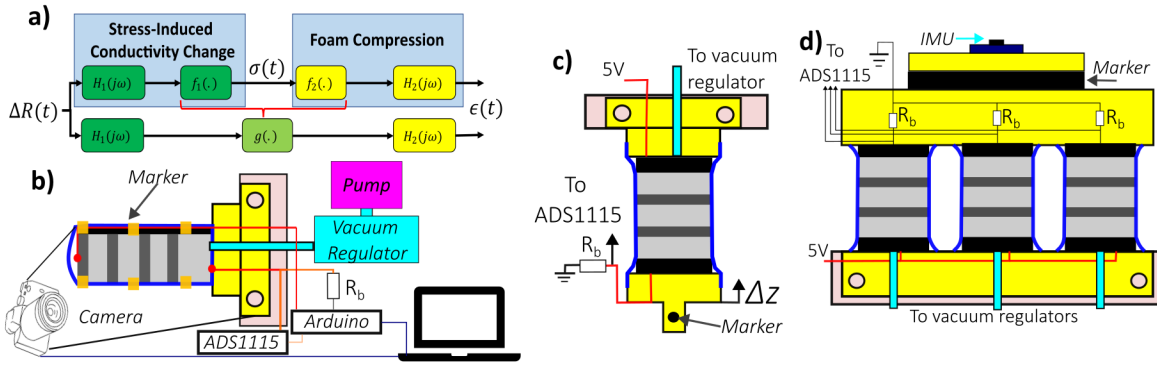


Figure 2: The pipeline for strain estimation (a) and the experimental setups: bending finger (b), single contractor (c), and 3DoF bending segment (d).

This model structure mimics the structure of the underlying physics. Firstly, the left part models the stress-driven resistance change<sup>26</sup>. Furthermore, it has been shown that the stress  $\sigma(t)$  is captured well by a Wiener model<sup>27</sup>

$$\sigma(t) = f_1((H_1(j\omega) \Delta R(t))) \quad (2)$$

The functions  $f_1$  and  $H_1(j\omega)$  represent a nonlinear mapping and linear transfer function, respectively. The first stage of the model relates the resistance change and stress. The stress and strain are also nonlinearly related for porous structures<sup>14,28,29</sup>. One possible approximation is through a nonlinear viscoelastic model to relate the strain to stress<sup>29</sup>. Within this work, a Hammerstein (HS) model is used as an approximation of the strain  $\epsilon(t)$

$$\epsilon(t) = H_2(j\omega) f_2(\sigma(t)) \quad (3)$$

Within this equation, the functions  $f_2$  and  $H_2(j\omega)$  represent a nonlinear mapping and a viscoelastic model (transfer function), respectively. Combining these two equations in series leads to the following equation

$$\epsilon(t) = H_2(j\omega) (g(H_1(j\omega) \Delta R(t))) \quad (4)$$

Within this equation, the two-stage static nonlinearity (i.e.  $f_1(f_2(\cdot))$ ) is reduced to a single one  $g(\cdot)$ . This function  $g(\cdot)$  approximates the combined nonlinear functions. Within this work,  $g(\cdot)$  was implemented as a piecewise linear function. This function type was selected as it fitted well with our data, and has seen use before in<sup>27</sup> for stress estimation. Lastly, it should be noted that the model in Equation 4 can be reduced to an HS or Wiener model by either removing  $H_2(j\omega)$  or  $H_1(j\omega)$ , respectively.

## 2.2 Fabrication of Sensorized Graded Actuators

All actuators in this work were fabricated using the InFoam method<sup>14</sup>. The InFoam method exploits the liquid rope coiling effect to print structures with a porosity gradient. Specifically, it uses the coils to create pores leading to a structure with programmable porosity (Fig. 1(e)). The coiling radius  $R_c$  and coiling density  $N$  define the coiling

pattern, which is machine specific and is determined by the height  $H$  and extruded amount. The coiling density  $N$  is the number of coils within a single outer coil diameter<sup>14</sup>. The relation between these parameters and the machine was determined through the method described in<sup>14</sup>. Subsequently, the InFoam method was used to generate the GCode through a custom MATLAB (The Mathworks, Inc., USA) script. The bending, contracting, and 3DoF bending segment actuators (Fig. 1)(a-c)) were fabricated using a modified Creality Ender 5 Plus (Shenzhen Creality 3D Technology Co., Ltd., China). This modified printer incorporated a screw extruder to enable the usage of thermoplastic elastomers. For this work, we used TC7OEX-BLCK pellets (Kraiburg TPE, Germany) with a Shore Hardness of 70A and a volume resistivity of  $10 \Omega\text{cm}$ , which were printed at  $195^\circ\text{C}$  with a 0.6 mm nozzle. For this material, the coiling radius and height were determined to fit a linear function as  $R_c = 0.40H - 0.3$  (range 2.5 to 10 mm) based on the methodology of<sup>14</sup>. In addition, to compute the porosity ( $\phi$  in %) the bulk density ( $\rho_b = 0.97 \text{ g/cm}^3$ ) was used in conjunction with the measured weight ( $m$  (g)) and volume of printed cubes ( $V$  ( $\text{cm}^3$ )) using  $\phi = 100 \left(1 - \frac{m}{V\rho_b}\right)$  (rounded to the nearest whole number). Lastly, the actuators were put into 0.4 mm thick heat-sealed styrene-ethylene-butylene-styrene (SEBS) to finalize the actuator.

### 2.3 Curvature Sensing

To investigate the capability of curvature sensing, a sensorized bending actuator was characterized. This bending actuator is based on the design of Fig. 1(a) and with dimensions  $75 \times 15 \times 10 \text{ mm}^3$  (length x width x height). For grading a 1 mm thick zero porosity layer, low (below 5%) porosity spacers, and a high porosity section of 84%. Electrodes (copper wires) were connected to the top left and bottom right of the actuator (Fig. 2(a)).

This experiment was performed using the setup shown in Fig. 2(b-d). The bending actuator was put into a holder printed from polylactic acid (PLA). Subsequently, the bending actuator was exposed to four levels of vacuum pressure (10, 20, 40, and 60 kPa). The pressure was applied in on/off pulses of ten seconds for three cycles (repeated in duplicate). During these experiments, the resistance change was measured using an Arduino Uno (Arduino AG, Italy) through a voltage divider and sent over serial to MATLAB. This voltage divider consisted of a bias ( $R_b$ ) resistor of  $1\text{k}\Omega$ , which was fed to an ADS1115 16-bit analog to digital converter (Texas Instruments, USA). In addition, a second experiment was conducted with a ramp of vacuum pressure from 10 up to 60 kPa (with a ten-second hold at 20, 40, and 60 kPa), after which the pressure was ramped down to 10 kPa (with ten second holds at the same pressures).

Lastly, a webcam was used to capture images of the actuator during the experiments. Trackers were added to the sleeve, in the form of black stripes, to reconstruct the curvature to act as the ground truth. Afterwards, MATLAB was used to reconstruct the curvature over time by computing a circle that fits the markers. Subsequently, the models were estimated using the curvature and resistance change through MATLAB's System Identification Toolbox. The NRMSE (normalized root mean square) fits of the model were evaluated through MATLAB's compare-function as:

$$NRMSEfit = 100 \left(1 - \frac{\|y - \hat{y}\|}{\|y - \bar{y}\|}\right) \quad (5)$$

In this equation, the NRMSE fit is computed using the two norm of the measured  $y$  and predicted  $\hat{y}$  output divided by the difference between the estimated value and average output  $\bar{y}$ . Similarly, the RMS error was computed and scaled by the maximum output (and the number of data points  $N$ ) in the dataset  $RMS = \frac{100}{\max(y)} \sqrt{\frac{\sum_{i=1}^N (y(i) - \hat{y}(i))^2}{N}}$ .

Four types of models were identified, namely: linear, HS, Wiener, and Wiener-Hammerstein (i.e Eq. 4). The latter was acquired by first identifying a Wiener/linear model and then using that as a filter to refine the output by adding a linear/HS model in series. All WH models use piece-wise linear functions as the nonlinear functions with five to ten breakpoints. The data was separated into an identification (ramp and the 60/10 kPa) and validation set (20 and 40 kPa).

### 2.4 Contraction Sensing

Besides curvature, the capability to predict/sense contraction was also investigated. Specifically, a set of contractors were investigated for their stroke and resistance change for multiple levels of porosity. Specifically, contractors based on the coiling pattern at heights of 4, 6, 8, and 10 mm and a coiling density of 3 (equivalent to porosities of 68, 76, 82, and 86%). All contractors were printed with a diameter of 25 mm and a total height of 45 mm. The graded porous section (Fig. 1(b)) had a height of around 40 mm and a low porosity (less than 5%) top and end cap (both 4 mm thick). The graded porosity section had two zero porosity rings at heights of 14 and 28 mm, which had a width of 5.6 mm.

The experimental protocol is identical to that of the curvature sensing. However, the setup is different as can be seen in Fig. 2(c). The contractor is hung in line with gravity and only a single marker was used. The identification approach was also kept the same but performed only for a low and high-porosity contractor. In addition, the experiments were performed for three load cases: no load, a 200-gram weight, and a dumbbell (500 grams).

## 2.5 Three Degree-Of-Freedom Bending Segment

To validate our approach for a more complex system with multiple inputs and outputs was investigated namely, a three DoF bending segment with three contractors in parallel (Fig. 1(c)). Three contractors were printed with the same dimension as indicated in the previous section with a porosity of 76%. Whereas the output, middle, and bottom stages were printed with PLA. The bottom and middle stages were spaced on an equilateral triangle with lengths of 30 mm. Whereas the spacers (below the black marker) have a length of 15 mm and the output stage on top is an equilateral triangle (length of 52 mm) with rounded edges.

For this experiment, a setup with three vacuum inputs and three resistance measurements (Fig. 2(d)) was used. Similar to the other setups, bias resistors of  $1k\Omega$  and the ADS1115 were used. To measure the orientation of the bending segment an IMU (a 9DOF absolute orientation BNO055 (Bosch Sensortec, Germany)) on a breakout board (Adafruit, USA) was used (with axis definition of Fig. 1(c)). The IMU and ADS1115 were connected to an Arduino Uno, which was used for sending data over serial to MATLAB. A black marker was added, (Fig. 2(c)) to track the height change using a webcam. As an input, both sequential and parallel activation patterns of the contractors were used. Either one, two, or three contractors were activated at 10, 20, 40, and 60 kPa. Within these experiments, cycles of 10 seconds pressure on/off for three times were performed (repeated in duplicate). In another pattern, two contractors were activated with one at vacuum pressures of [10, 20, 30] and one at [40, 60] kPa. The timings for the high and low-pressure contractors were (5,25,45)/(15,35,55) (turn on/off) and (5,45)/(35,65), respectively. The data from these experiments were used for the identification of three models, i.e. one for each output. The same set of models as for the other systems was identified and validated.

## 3 Results and Discussion

### 3.1 Curvature Sensing

The curvature versus change in resistance is shown in Fig. 3. It can be observed that there is hysteresis in all three scenarios. This behavior means a simple relationship between resistance change and curvature does not exist but is dependent on history. The area of hysteresis seems to not be dependent on the magnitude of the vacuum pressure as the 10 kPa seems to have more hysteresis than the ramp even though the latter reaches 60 kPa. The slower increase in pressure in the ramp dataset implies that the rate could play a significant factor. Such behavior is expected, as existing models of carbon black-based piezo-resistive sensors include a damping component<sup>26</sup>. Thereby implying that the rate does play a role in the observed behavior and that a proper model of these sensors will need to take the history into account, which the Wiener-Hammerstein model can do.

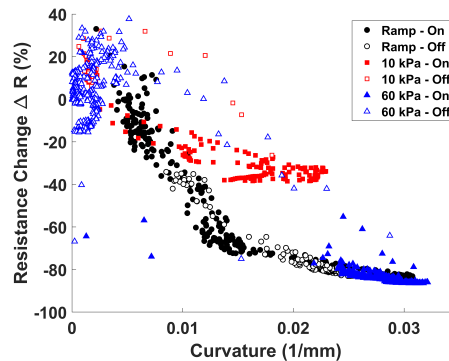


Figure 3: Hysteresis curve of resistance change versus curvature with pressure turn on/off indicated.

A set of models were estimated based on the identification datasets (one for each model type). These models were evaluated based on their average NRMSE fit and the best one was kept. The predictions of these identified models are shown in Fig. 4, which includes a set from identification and two validation sets. It can be seen that all models can capture the dynamics of the ramp dataset quite well. In line with our hypothesis, the WH model outperforms the other three. Whereas the Wiener and HS have a lower fit than the linear model only for the ramp dataset. However, looking at how well they approximate the curve the linear model just averages whereas the nonlinear models try to capture the faster dynamics and nonlinearities. This discrepancy is especially apparent in the other two datasets (i.e. the validation). The fits for 20 kPa clearly show that the linear model has significant problems with capturing the dynamics properly leading to overshooting. However, this difference is significantly less apparent for the 40 kPa dataset instead of 40% it

differs only 10.6% with the WH-model. Whereas the HS and Wiener model is around 30 and 9% better, which indicates that the nonlinear models generalize better.

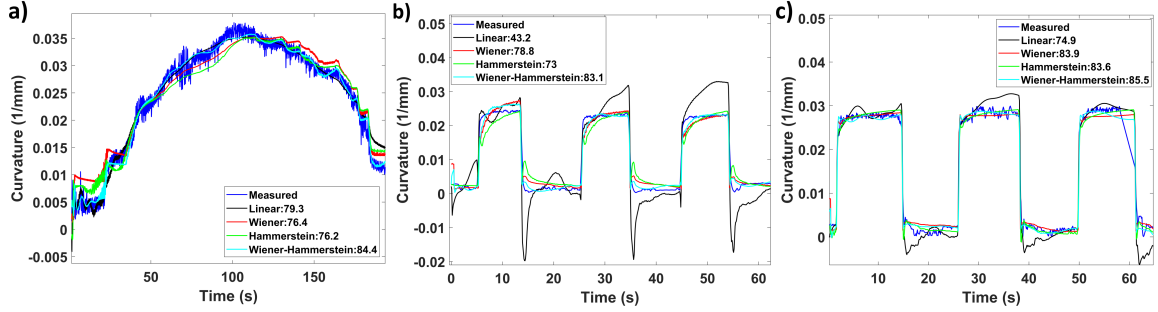


Figure 4: Real and predicted curvature (incl. NRMSE fit in legend) for (pressure) ramp dataset (a) and validation datasets (20 (b) and 40 (c) kPa).

It is expected that the error is much less for the 40 kPa dataset as foam-like structures collapse and have distinct regimes of change. These distinct regimes have a rapid and large change when the pores collapse<sup>20</sup> followed by a slower decrease in resistance after the air is pushed out. It is expected that the linear approximation between the datasets of 10 kPa and 60 kPa does approximate the 40 kPa-dataset well but not the 20 kPa, which implies that the densification within that range.

The overall identification results are summed up in Table 1. It can be seen that on average all the models capture the dynamics quite well. It can be observed that refining the WH model reduces the fitting error by 21.4% (i.e. error decreased from 19.6 to 15.4%). In addition, the WH model seems better in general than the Wiener model. The Wiener model has fits that vary from 72.4-90.7% whereas the WH model has a much narrower range of 80.2-90.0%. This behavior is to be expected, as the linear model would average the error out (see for instance the ramp signal). The RMS error (normalized by the maximum curvature) of the models was computed to be:  $5.2 \pm 1.4$ ,  $6.5 \pm 1.9$ ,  $7.0 \pm 2.7$ , and  $10.42 \pm 7.98\%$  for the WH, Wiener, HS, and linear models, respectively, which values indicate that the nonlinear models are better estimators.

Table 1: NRMSE fits for the bending actuator.

Type	Ramp	10	60	20	40	Avg.
Linear	79.3%	76.3%	84.7%	43.2%	74.9%	71.7%
Wiener	76.4%	72.4%	90.7%	78.8%	83.9%	80.4%
HS	76.2%	77.8%	87.8%	73.0%	83.6%	79.7%
WH	84.4%	80.2%	90.0%	83.2%	85.5%	84.6%

These results imply that WH and its variation can provide a reasonable estimation of the curvature. Whereas nonlinearities are necessary to compensate for the nonlinear relation between resistance change and curvature in general. The piezoresistive sensorized actuator's ability to estimate its strain indicates that it performs (at least) on par with the works primarily focussed on empirical behavior of foam-like porous sensors and sensorized actuators<sup>16,19,20,21</sup>. Whereas the sensorized piezoresistive bellow<sup>13</sup> was comparable in terms of estimation errors (albeit for the force) with around 4% (they did not report a value for position estimation). Similarly, in<sup>27</sup> a 90% fit was acquired for stress estimation but using a commercial force sensing resistor, which makes absolute comparisons difficult. However, similar to their result the Wiener/HS models provide much better results than those seen with linear models. In addition, our results indicate that the WH, for strain estimation, is a better model structure. Lastly, other researchers have shown better results for other sensor types, such as twisted-coiled actuators<sup>11</sup>, reported RMSE below 1% but with low sensitivity (resistance change/strain of  $0.83 \Omega$  with a maximum of 25%). Thereby implying piezoresistive sensing could have some advantages but efforts need to be made for improving accuracy.

### 3.2 Contraction Sensing

The averaged strain and resistance change for all contractors is shown in Fig. 5 for different load cases. Within the six pressure cycles the maximum strain varied less than 10% and was, therefore, not added to the graphs. In general, a similar trend can be seen for all data points. In general the compressive strain and resistance change increase with increasing porosity and pressure. In contrast, the increase of a load negatively impacts the strain but the resistance change is less affected. This discrepancy implies that the relation between strain and resistance change is load dependent. The nonlinear decrease of the resistance with the contractor's deformation is shown in Fig. 1(d).

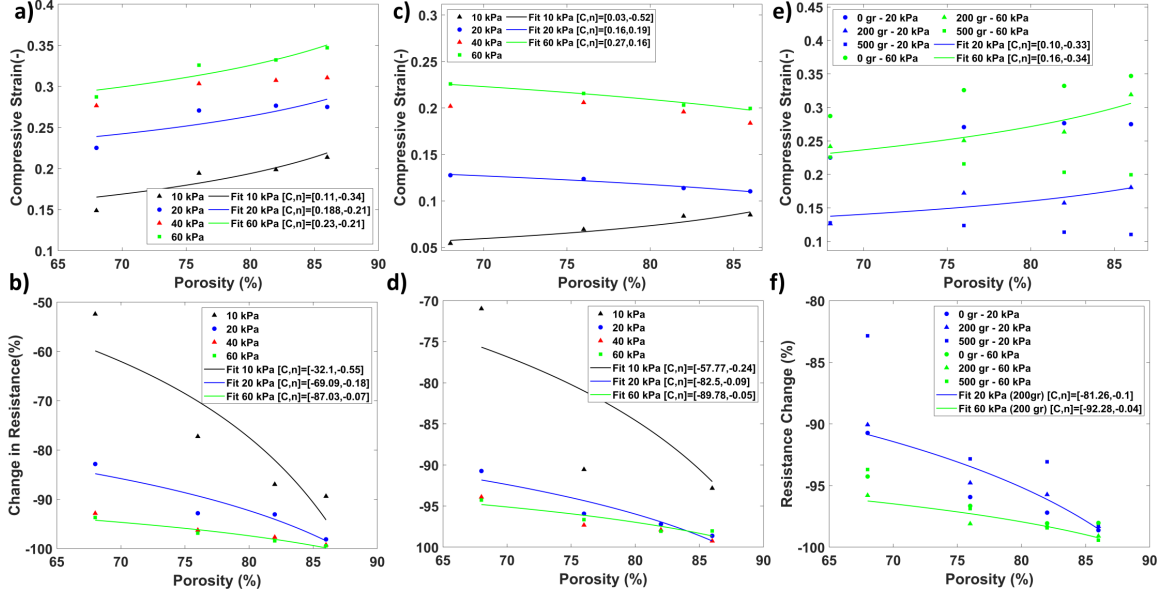


Figure 5: Strain/resistance change versus porosity with fitted power law curve (with parameters in legend) for different vacuum pressures for the case of no load (a,b), a 500 grams load (c,d), and multiple load cases for two vacuum pressures (e,f) for the contractor system.

Higher porosity coincides, in general, with a higher change in resistance, which is to be expected as the final shape is smaller and the contact area increases more significantly. However, this increase does not correlate with a higher strain sensitivity for the 500 gr load. This contradiction is expected to be due to the load's effect on the contractor's stiffness. The addition of a load will increase the longitudinal stiffness as a constant force spring but not the radial stiffness. At a certain load, the radial stiffness will be lower than the longitudinal. At that point, the collapse will be more radially. Thereby still reducing the resistance significantly but reducing the strain. Such change is more apparent for the higher porosity (softer) actuators as these have a lower radial stiffness overall.

Interestingly, the trends of both the change in resistance and strain can be approximated by a power-law  $p_f = C(1 - \phi/100)^n$ . Within this equation, variables  $p_f$ ,  $\phi$ ,  $C$ ,  $n$  represent the property of interest of the porous structure, the porosity (%), and two fitting parameters. It has been shown that this power law can estimate changes in mechanical properties (yield stress, density, elastic modulus) of cellular solids (such as foams)<sup>30</sup> and mechanical programming of soft actuators<sup>14</sup>. Similarly, the results of Fig. 5(a-f) show that this empirical law approximates the strain change for different loads quite well. Similarly, the change in resistance also fits this empirical quite well. The general behavior is similar to the result of<sup>19</sup>, which also showed increased sensitivity to pressure with increasing porosity. These results provide evidence that the porosity can be used as a tool to program both the strain but also its sensitivity (i.e. resistance change). This power-law behavior with porosity was also seen for the behavior of a bending actuator in our earlier work<sup>14</sup>. Although for low vacuum pressures (i.e.  $\leq 20$  kPa) this approximation seems less correct. In addition, it can be observed that the contractors have a higher sensitivity than the proprioceptive bellow of<sup>13</sup> with values exceeding 4.5%.

All models were identified separately for the no load and 500 grams. This change was mandatory based on the results of Fig. 5. This identification approach gave the results of Fig. 6(a-c) for the 40 kPa validation dataset, which indicates overall good NRSME fits for all models. Although the lines in Fig. 6(a) seems to qualitatively approximate it well there are some discrepancies. However, in steady-state these are at most a strain error of 0.02 (around 8.7% of the strain magnitude), which still seems a reasonable prediction. The results of the average NRSME fit are shown in Table 2. In general, the NRMSE fits of the WH model outperformed the others. Although it can be noted that the others were still good. But overall the WH model reduced the fitting error of the linear/Wiener/HS model from 22.5/19.0/18.0% to 14.4% a fitting error reduction of 36.1/24.3/20.1%. Implying that the WH model's structure correlates better with the underlying physics.

Lastly, the RMS error (normalized by the maximum strain) is averaged over all three datasets [8.7, 7.1, 7.3, 5.8]% for the linear, HS, Wiener, and WH models, respectively. These values indicate an overall good estimation of the models with the nonlinear models performing better and WH being the best overall. Lastly, it can be observed that this data corroborates the discussion of the previous section, further providing evidence that the WH model is an appropriate structure for strain estimation with piezoresistive sensors.

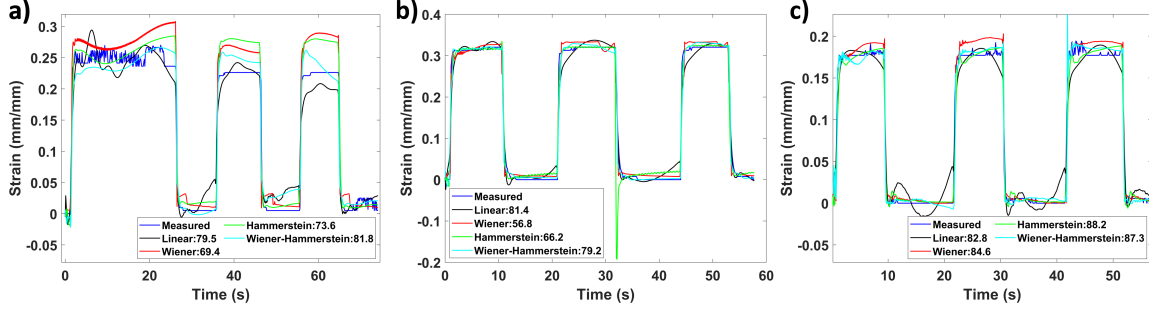


Figure 6: Measured and estimated contraction (with NRMSE fit in the legend) of identified models for the contractor system for the 40 kPa datasets (validation) for a low porosity (68%) with no load (a) and 500 gr (b) and the high porosity (82%) no load (c).

Table 2: Averaged NRMSE fits for the contractor.

Type	Low - no-load	Low - 500 gr	High - no-load
Linear	75.5/67.7%	73.2/78.5%	86.1/83.0%
Wiener	76.4/74.7%	86.7/83.6%	88.3/72.3%
Hammerstein	80.6/76.4%	84.4/86.2%	84.9/77.7%
WH	83.1/76.7%	88.4/86.7%	91.2/84.8%

### 3.3 Three Degree-Of-Freedom Bending Segment

The realized 3DoF bending segment could bend ( $\theta_x, \theta_y$ ) for 26.3/22.6 degrees. Whereas it had a maximum  $\Delta z$  of 16 mm (axis definition in Fig. 1(c)). Three individual identification (one for each deformation) were performed with input (the three resistance changes) and outputs ( $\theta_x, \theta_y, \Delta z$ ). The acquired predictions for these identified models are seen in Fig. 7. The HS models had NRMSE fits below 70% and were omitted. In general, the linear and WH models seem robust, as they stay around similar levels for all cases. In contrast, the Wiener model dips below 60% and for some datasets (not shown) below 40%. However, for the steady state situations, the WH-model and Wiener models perform better than the linear model. This discrepancy is especially visible in the oscillations that the linear models predict during steady state. In general, the overall behavior seems better captured by the WH model.

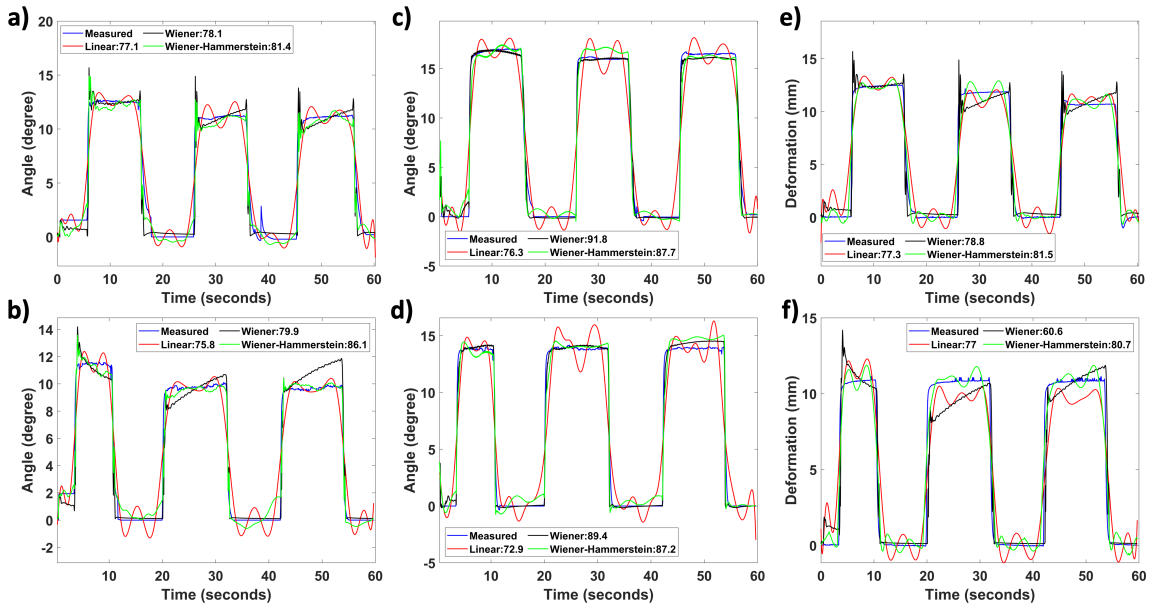


Figure 7: Measured and predicted angle of the 3DoF bending segment in the  $x$ -(a,b) and  $y$ -(c,d)-direction and deformation in  $z$  (e,f) from the identification (a,c,e) and validation (b,d,f) dataset with their NRMSE fits included in the legend. The NRMSE fit was computed by averaging the identification and validation datasets NRMSE fits, which are shown in Table 3. It can be noted that the NRMSE fit is better for the WH model but not the Wiener model. A possible reason for



this discrepancy is that the actuator is nonlinearly related to the contraction of an individual contractor<sup>31</sup>, which might not be captured well by a Wiener model. Similarly, the RMSE (normalized by maximum bending/deformation within each experiment) is  $7.4\pm 0.9/6.1\pm 1.9$  and  $8.4\pm 1.7$  % for the WH whereas the linear model was  $10.1\pm 0.8/9.5\pm 1.1$  and  $9.9\pm 1.0$  %. Implying again that the WH model is a good option for these systems.

Table 3: NRMSE fits for the 3DoF bending segment actuator.

Type	$\theta_x$	$\theta_y$	$\Delta z$
Linear	$76.0\pm 1.5\%$	$77.44\pm 2.6\%$	$76.38\pm 1.95\%$
Wiener	$76.7\pm 6.8\%$	$80.4\pm 14.9\%$	$51.53\pm 21.4\%$
WH	$82\pm 2.3\%$	$79.4\pm 9.8\%$	$80.6\pm 2.8\%$

In general, these results corroborate that the sensorized actuators can reconstruct their state. The multi-input and output system corroborates the results for the bending actuator and contractor, which implies that the WH model is an appropriate model structure. In addition, it goes beyond the works discussed previously, which focused on single input-output systems, and shows that our approach generalizes to more complex strain estimation problems.

## 4 Conclusion

Sensor-integrated soft actuators have the potential to be used in a broad range of applications as they inherently provide proprioceptive data. By providing proprioceptive data these actuators can sense their deformation, which can be used for, for instance, feedback control. Within this work, we have demonstrated that the InFoam method can 3D print conductive thermoplastic elastomers with a user-defined porosity gradient to combine actuation and sensing. The ability to fabricate these sensorized actuators using 3D printing allows for significant design freedom and flexibility. In essence, the presented results show that the InFoam can print mechanically programmable sensorized actuators. The measured change in resistance of these sensorized 3D printed actuators can be fed into an estimated Wiener-Hammerstein model to estimate the strain behavior over time ( $\geq 80\%$ ), which was significantly better than linear models in most cases. The results in this paper indicate that the Wiener-Hammerstein model is viable for different levels of porosity, motion (curvature and translation), and multiple degrees of freedom (3DoF bending segment). In general, the WH model could compensate for the nonlinearities and hysteresis of the sensorized actuator. It is expected that other piezoresistive sensors could also use this model structure, as it correlates with the underlying physics. When combined with data-driven techniques (such as Wiener-Hammerstein models) the measurement data can be used to estimate the strain. However, the accuracy can still be improved significantly. The next step is to integrate multiple outputs to accurately reconstruct the deformation of the actuator. The current implementation assumes that deformation is solely due to the actuator, which as seen with the radial collapse of the contractor makes the accuracy load dependent.

## References

- [1] D. Trivedi, C. D. Rahn, W. M. Kier, and I. D. Walker, "Soft robotics: Biological inspiration, state of the art, and future research," *Applied bionics and biomechanics*, vol. 5, no. 3, pp. 99–117, 2008.
- [2] H.-T. Lin, G. G. Leisk, and B. Trimmer, "Goqbot: a caterpillar-inspired soft-bodied rolling robot," *Bioinspiration & biomimetics*, vol. 6, no. 2, p. 026007, 2011.
- [3] C. Laschi, M. Cianchetti, B. Mazzolai, L. Margheri, M. Follador, and P. Dario, "Soft robot arm inspired by the octopus," *Advanced robotics*, vol. 26, no. 7, pp. 709–727, 2012.
- [4] Y. Kumaresan, O. Ozioko, and R. Dahiya, "Multifunctional electronic skin with a stack of temperature and pressure sensor arrays," *IEEE Sensors Journal*, vol. 21, no. 23, pp. 26 243–26 251, 2021.
- [5] S. Li, D. M. Vogt, D. Rus, and R. J. Wood, "Fluid-driven origami-inspired artificial muscles," *Proc. of the National academy of Sciences*, vol. 114, no. 50, pp. 13 132–13 137, 2017.
- [6] F. Connolly, P. Polygerinos, C. J. Walsh, and K. Bertoldi, "Mechanical programming of soft actuators by varying fiber angle," *Soft Robotics*, vol. 2, no. 1, pp. 26–32, 2015.
- [7] B. Mosadegh *et al.*, "Pneumatic networks for soft robotics that actuate rapidly," *Adv. Funct. Mater.*, vol. 24, no. 15, pp. 2163–2170, 2014.
- [8] D. R. Higuera-Ruiz, K. Nishikawa, H. Feigenbaum, and M. Shafer, "What is an artificial muscle? a comparison of soft actuators to biological muscles," *Bioinspiration & biomimetics*, vol. 17, no. 1, p. 011001, 2021.
- [9] W. Felt, K. Y. Chin, and C. D. Remy, "Contraction sensing with smart braid mckibben muscles," *IEEE/ASME Transactions on Mechatronics*, vol. 21, no. 3, pp. 1201–1209, 2015.

- [10] E. Acome *et al.*, “Hydraulically amplified self-healing electrostatic actuators with muscle-like performance,” *Science*, vol. 359, no. 6371, pp. 61–65, 2018.
- [11] J. Sun and J. Zhao, “Integrated actuation and self-sensing for twisted-and-coiled actuators with applications to innervated soft robots,” in *2020 IEEE/RSJ Int. Conf. on Intell. Robots and Syst. (IROS)*. IEEE, 2020, pp. 8795–8800.
- [12] K. Kure, T. Kanda, K. Suzumori, and S. Wakimoto, “Flexible displacement sensor using injected conductive paste,” *Sensors and Actuators A: Physical*, vol. 143, no. 2, pp. 272–278, 2008.
- [13] J. Zhou, Y. Chen, X. Chen, Z. Wang, Y. Li, and Y. Liu, “A proprioceptive bellows (pb) actuator with position feedback and force estimation,” *IEEE Robot. and Automat. Letters*, vol. 5, no. 2, pp. 1867–1874, 2020.
- [14] N. Willemstein, H. van der Kooij, and A. Sadeghi, “3d printing of soft fluidic actuators with graded porosity,” *Soft matter*, vol. 18, no. 38, pp. 7269–7279, 2022.
- [15] M. A. Robertson and J. Paik, “New soft robots really suck: Vacuum-powered systems empower diverse capabilities,” *Science Robotics*, vol. 2, no. 9, p. eaan6357, 2017.
- [16] S. P. Murali Babu, F. Visentin, A. Sadeghi, A. Mondini, F. Meder, and B. Mazzolai, “Sensorized foam actuator with intrinsic proprioception and tunable stiffness behavior for soft robots,” *Advanced Intelligent Systems*, vol. 3, no. 6, p. 2100022, 2021.
- [17] B. C. Mac Murray *et al.*, “Poroelastic foams for simple fabrication of complex soft robots,” *Adv. Mat.*, vol. 27, no. 41, pp. 6334–6340, 2015.
- [18] I. Van Meerbeek, C. De Sa, and R. Shepherd, “Soft optoelectronic sensory foams with proprioception,” *Science Robotics*, vol. 3, no. 24, p. eaau2489, 2018.
- [19] S. Bilent, T. H. N. Dinh, E. Martincic, and P.-Y. Joubert, “Influence of the porosity of polymer foams on the performances of capacitive flexible pressure sensors,” *Sensors*, vol. 19, no. 9, p. 1968, 2019.
- [20] M. Pruvost, W. J. Smit, C. Monteux, P. Poulin, and A. Colin, “Polymeric foams for flexible and highly sensitive low-pressure capacitive sensors,” *npj Flexible Electronics*, vol. 3, no. 1, pp. 1–6, 2019.
- [21] S. Nakamaru, R. Nakayama, R. Niiyama, and Y. Kakehi, “Foamsense: Design of three dimensional soft sensors with porous materials,” in *Proceedings of the 30th Annual ACM Symposium on User Interface Software and Technology*, 2017, pp. 437–447.
- [22] J. Cheng, M. Sundholm, B. Zhou, M. Hirsch, and P. Lukowicz, “Smart-surface: Large scale textile pressure sensors arrays for activity recognition,” *Pervasive Mob. Comput.*, vol. 30, pp. 97–112, 2016.
- [23] N. M. Ribe, M. Habibi, and D. Bonn, “Liquid rope coiling,” *Annual review of fluid mechanics*, vol. 44, pp. 249–266, 2012.
- [24] J. I. Lipton and H. Lipson, “3d printing variable stiffness foams using viscous thread instability,” *Sci. Rep.*, vol. 6, no. 1, pp. 1–6, 2016.
- [25] W. Felt, M. A. Robertson, and J. Paik, “Modeling vacuum bellows soft pneumatic actuators with optimal mechanical performance,” in *2018 IEEE Int. Conf. on Soft Robot. (RoboSoft)*. IEEE, 2018, pp. 534–540.
- [26] L. Paredes-Madrid, C. A. Palacio, A. Matute, and C. A. Parra Vargas, “Underlying physics of conductive polymer composites and force sensing resistors (fsrs) under static loading conditions,” *Sensors*, vol. 17, no. 9, p. 2108, 2017.
- [27] M. Y. Saadeh and M. B. Trabia, “Identification of a force-sensing resistor for tactile applications,” *Journal of Intelligent Material Systems and Structures*, vol. 24, no. 7, pp. 813–827, 2013.
- [28] Q. Liu and G. Subhash, “A phenomenological constitutive model for foams under large deformations,” *Polymer Engineering & Science*, vol. 44, no. 3, pp. 463–473, 2004.
- [29] V. Goga, “New phenomenological model for solid foams,” in *Computational modelling and advanced simulations*. Springer, 2011, pp. 67–82.
- [30] I. Gibson and M. F. Ashby, “The mechanics of three-dimensional cellular materials,” *Proc. R. Soc. A: Math. Phys. Eng. Sci.*, vol. 382, no. 1782, pp. 43–59, 1982.
- [31] T. F. Allen, L. Rupert, T. R. Duggan, G. Hein, and K. Albert, “Closed-form non-singular constant-curvature continuum manipulator kinematics,” in *2020 3rd IEEE International Conference on Soft Robotics (RoboSoft)*. IEEE, 2020, pp. 410–416.